Rock Mechanics and Rock Engineering
https://doi.org/10.1007/s00603-023-03529-3

ORIGINAL PAPER

Self-Sealing of Boom Clay After Gas Transport

Laura Gonzalez-Blanco[1,2] · **Enrique Romero**[1,2] · **Séverine Levasseur**[3]

Received: 19 December 2022 / Accepted: 23 August 2023

Abstract

In the geological disposal of high-level radioactive waste in argillaceous rocks, studying the barrier integrity after gas transport and the pathway closure thanks to self-sealing capacity is a crucial aspect for the safety assessment. This paper presents experimental research in Boom Clay (a potential host rock in Belgium) to evaluate the effectiveness of self-sealing and possible fissure reactivation during a second gas invasion event. Initial water permeability under oedometer conditions was first measured on samples at two bedding orientations, being higher the sample with bedding planes parallel to flow, highlighting marked anisotropy. Then, gas injection tests at a constant volume rate were performed. Results indicated that Boom Clay underwent expansion and degradation during gas injection due to the development of fissures that were quantified using microstructural techniques. The computed effective gas permeability was not significantly dependent on bedding orientation and was slightly larger than the initial intrinsic water permeability. The re-saturation of the samples led to a recovery of the initial water permeability for both orientations, replicating the original anisotropy. The microstructural analyses confirmed the gas pathways' closure, indicating good self-sealing and the regaining of the hydraulic barrier function. However, a small volume of large unconnected pores was detected on undrained unloading before the microstructural study. An additional gas injection after the self-sealing resulted in a higher effective gas permeability and a larger increase in pore volume, suggesting the reopening of fissures generated during the first injection. Finally, the experimental data were compiled within a multi-scale phenomenological model to relate the microstructural information to macroscopic flow transport properties capturing the intrinsic permeability increase on gas invasion and its recovery during self-sealing.

Highlights

- Gas transport on Boom Clay occurs along fissures, increasing its permeability
- The re-saturation process induces the recovery of the initial water permeability, demonstrating an excellent self-sealing capacity.
- A subsequent gas injection after the re-saturation suggests the reopening of previous gas paths.
- A multi-scale model is proposed to account for the permeability changes derived from a microstructural damage variable.

✉ Laura Gonzalez-Blanco
laura.gonzalez.blanco@upc.edu

Enrique Romero
enrique.romero-morales@upc.edu

Séverine Levasseur
s.levasseur@nirond.be

[1] Division of Geotechnical Engineering and Geosciences, Department of Civil and Environmental Engineering, Universitat Politècnica de Catalunya, C/Jordi Girona 1-3, Campus Nord UPC, Building D-2, 08034 Barcelona, Spain

[2] Geomechanics Group, International Centre for Numerical Methods in Engineering (CIMNE), c/Gran Capità S/N, Campus Nord UPC, Building C-1, 08034 Barcelona, Spain

[3] Belgian Agency for Radioactive Waste and Enriched Fissile Materials (ONDRAF/NIRAS), Avenue Des Arts 14, 1210 Brussels, Belgium

Published online: 22 September 2023

Keywords Radioactive waste disposal · Gas transport · Permeability · Preferential gas pathways · Self-sealing · Microstructural analysis

List Of Symbols

A	Area of the sample
D	Damage variable
e	Void ratio
e_{av}	Average void ratio
e_f	Fissured void ratio (volume of fissures to the volume of solids)
e_M	Macro-void ratio (volume of macro-pores to the volume of solids)
f	Macro-fissured ratio (volume of macro-pores and fissures to the volume of voids)
f_0	Volume of the macro-pores to the volume of voids at the intact state
e_{nw}	Non-wetting void ratio (MIP)
g	Acceleration of gravity
k_a	Air permeability
k_w	Water permeability
k_i	Intrinsic permeability
$k_i k_r$	Effective permeability
$k_{initial}$	Initial value of intrinsic water permeability
k	Permeability measured during the last stage of the tests
k_r	Relative permeability
L	Length of the sample
n	Porosity
PSD	Pore size density function
s	Total suction
S_r	Degree of saturation
t	Time
$\overline{u}_a$	Absolute air pressure of the upstream reservoir
$\overline{u}_{at}$	Absolute air pressure of the downstream reservoir
u_w	Pore water pressure
V	Volume of the upstream reservoir
V_s	Volume of solids
V_m	Volume of micro-pores
V_M	Volume of macro-pores
V_f	Volume of fissures
V_{total}	Volume of the sample
w	Water content
w_L	Liquid limit
w_P	Plastic limit
x	Entrance pore size
α	Parameter of van Genuchten's equation
α_i	Constant parameter in Eq. (5)
ε_a	Axial strain
λ	Parameter of van Genuchten's equation
μ_a	Air dynamic viscosity at standard pressure and temperature
π	Osmotic suction
ρ_a	Air density at standard pressure and temperature
ρ	Bulk density
ρ_d	Dry density
ρ_s	Density of solids
σ_v	Total vertical stress
σ'_v	Effective vertical stress

1 Introduction

Sedimentary clayey formations have been studied during the last decades as host rocks for the geological disposal of long-living and heat-emitting radioactive waste. The argillaceous rocks present desirable characteristics, making them suitable for isolating and confining wastes during the operational life of the repositories. Their low permeability allows for reducing the transport of radionuclides, and their retention capacity delays the migration of contaminants (Nagra 2002; Andra 2005; Bernier et al. 2007b; ONDRAF/NIRAS 2013; Giger et al. 2015). However, the clayey rocks may present natural fractures such as geologic faults and/or induced fractures caused by the excavation activities during the repository construction, forming what is known as the excavation disturbed zone (EDZ). The presence of fractures can increase the hydraulic conductivity by several orders of magnitude while transporting radionuclides (NEA 2010). This is why the self-sealing or self-healing capacity of these rocks is a crucial issue for the safety assessment of the disposals. According to Bernier et al. (2007a), sealing is the reduction of fracture permeability by any hydro-mechanical, hydro-chemical, or hydro-biochemical process, while healing is the self-repair of cracks with loss of memory of the pre-healing state. The term self is defined as a healing or sealing process that happens spontaneously without human intervention. The physical mechanisms driving this phenomenon are mainly the swelling of clay minerals, the consolidation and the creep. However, it is often difficult to quantify the contribution of each of them and depends on the properties of the rock (Bastiaens et al. 2007).

The potential self-sealing/healing of the clayey host rocks has been experimentally studied concerning the fractures of the EDZ since the EC-funded SELFRAC project (Bernier et al. 2007a; Bastiaens et al. 2007; Van Geet et al. 2008). Laboratory tests were conducted on artificially created fractures subjected to different chemo–thermo–hydro-mechanical paths (Van Geet et al. 2008; Zhang 2011; Zhang et al. 2014; Honty et al. 2017; Giot et al. 2019; Voltolini and Ajo-Franklin 2020; Di Donna et al. 2022; Zhang and Talandier 2022), and the self-sealing/healing capacity was evaluated by comparing the permeability of the intact material with the one after the closure of the fracture and generally supported

with imaging techniques. Most results provided strong evidence for the high self-sealing capacity of different claystones rather than the complete self-healing.

Nonetheless, in the operational life of the repositories, the accumulation of gases, mainly due to the anaerobic corrosion of the metallic parts, could result in an excessive pressure build-up in these low-permeability and saturated media (Volckaert et al. 1998), leading to the generation of fractures/fissures or the reactivation of existing ones acting as preferential pathways for the gas flow (Cevatoglu et al. 2015; Cuss et al. 2014; Fall et al. 2014; Gerard et al. 2014; Gonzalez-Blanco et al. 2016, 2017, 2022; Liu et al. 2016a, b; Harrington et al. 2017; Senger et al. 2018; Levasseur et al. 2021; Gonzalez-Blanco and Romero 2022). Self-sealing of fractures is likely to occur, since gas migration pathways are usually considered transient (Levasseur et al. 2021). However, there is still a need to prove the effectiveness of the self-sealing process along gas-induced pathways. This is one of the objectives of the Work Package GAS of the European Joint Programme on Radioactive Waste Management (EURAD 2019) within this paper is framed.

To the authors' knowledge, there is scarce experimental data regarding this topic, but for Zhang and Talandier (2022), who studied the recovery of gas-induced pathways in previously fractured and sealed indurated clay samples, the Opalinus Clay (host rock considered in Switzerland) and the Callovo-Oxfordian Clay (host rock considered in France). These authors measured water permeability and compared it with that before gas penetration. In this paper, Boom Clay, a poorly indurated clay candidate in the Belgian programme, was experimentally studied using a similar approach. Intact Boom Clay samples, retrieved from the HADES underground research laboratory (URL) in Mol (Belgium) but far from the EDZ, were subjected to gas injection and then re-saturated to evaluate the self-sealing. Gonzalez-Blanco and Romero (2022) confirmed that Boom Clay undergoes expansion and degradation during gas injection due to the development of fissures quantified using microstructural techniques [mercury intrusion porosimetry (MIP), field-emission scanning electron microscopy (FESEM) and X-ray microtomography (μ-CT)]. The opening of gas pathways led to an increase in permeability. Therefore, the open question that this paper addresses is if these fissures can be sealed during a re-saturation stage, recovering the initial permeability. In addition, the possible fissure reactivation is investigated with a second gas injection after the sealing process. The permeability measurements of water and gas are accompanied by the evaluation of the microstructural features after each process. Finally, a model is proposed within a multi-scale perspective, integrating both macro-phenomenological processes of water and gas transport and microstructural information. The model can describe the change in permeability from the initial water permeability to the increase during the gas invasion and its recovery upon re-saturation in terms of a microstructural damage variable.

2 Soil Properties and Experimental Methods

2.1 Boom Clay Samples

The Boom Clay formation is a marine sediment of the Cenozoic, specifically of the Rupelian age (Northwest European Tertiary Basin, 36–30 My). Its mineralogical composition is homogeneous in the vertical profile being 20–30% kaolinite, 20–30% illite, 10–20% smectite, and 25% quartz and feldspar (Bernier et al. 2007b; Delage et al. 2007; Sultan et al. 2010). At the Mol-Dessel nuclear site (Belgium), the Boom Clay lies 160–270 m below ground level in almost horizontal layers (it dips 1–2% towards the NE), presenting depositional bedding planes in the horizontal direction, which lead to anisotropic features (Lima 2011; Salehnia et al. 2015; Gonzalez-Blanco et al. 2017). The samples used in this study were collected at a depth of 223 m in the horizontal plane of the Belgian underground research facility (URF), the HADES, and belong to Core 8 (Core Ref.: CG66-67W_Core8_Sectiona). At that depth, the total vertical stress and water pressure are around $\sigma_v = 4.6$ MPa and $u_w = 2.2$ MPa, respectively.

The basic properties of the intact material ("as-received") were determined in the laboratory and are shown in Table 1 compared to samples used in previous studies (Gonzalez-Blanco et al. 2016, 2022; Gonzalez-Blanco and Romero 2022). The samples of Core 8 presented a lower initial degree of saturation and higher total suction, possibly due to some desiccation during the storage, but still below the air-entry value determined from the water retention curve (air-entry value of around 4.6 MPa). Figure 1 presents the water retention capacity measured using a chilled mirror dew point psychrometer by stepwise drying from the initial total suction and a void ratio of 0.59, considering the shrinkage of the sample using data reported in Lima (2011).

2.2 Experimental Equipment and Protocol

The applied methodology aims at replicating the procedures followed in previous experimental campaigns in which the gas transport process and its consequences in terms of microstructure changes were studied, but this time, some additional steps have been included to evaluate the self-sealing capacity of the Boom Clay and the consequences of a subsequent gas injection after re-saturation. Therefore, the same high-pressure oedometer cell was used (Gonzalez-Blanco and Romero 2022). The samples of 50 mm in diameter and 20 mm in height were installed between the top and bottom caps to allow the injection and

Table 1 Main geotechnical properties and initial state of Boom Clay (BC) samples

Main properties/initial state	This study	Previous studies (Gonzalez-Blanco et al. 2016, 2022; Gonzalez-Blanco and Romero 2022)
Density of solids, ρ_s (Mg/m^3)	2.67	2.67
Liquid limit, w_L (%)	67	56
Plastic limit, w_P (%)	29	29
Bulk density, ρ (Mg/m^3)	2.05	2.02–2.06
Dry density, ρ_d (Mg/m^3)	1.67–1.68	1.63–1.69
Water content, w (%)	19.0–20.2	22.6–24.0
Void ratio, e	0.58–0.59	0.58–0.63
Porosity, n	0.37	0.37–0.39
Degree of saturation, S_r	0.93–0.96	1.0
Total suction, s (MPa)	3.2	2.45
Osmotic suction, π (MPa)	0.5	0.5

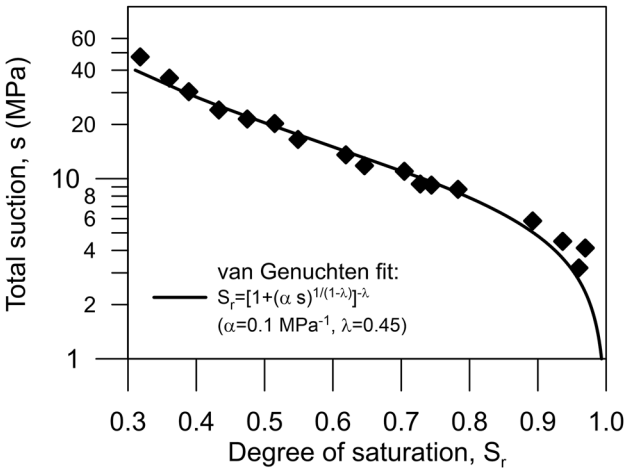

Fig. 1 Drying branch of the water retention curve fitted with van Genuchten's equation

recovery of water and gas. An external LVDT measured the vertical displacements. The vertical stress was applied using a pressure/volume controller (PVC). Water and gas flow at the bottom of the sample (upstream boundary) were imposed by two independent PVCs. The recovery line, connected to the top of the sample (downstream boundary), consisted of another PVC to collect water or gas and apply the outflow pressure.

In addition, MIP (Romero and Simms 2008) and μ-CT (Cnudde and Boone 2013; Paul et al. 2019) were used as integrated microstructural techniques to observe the evolution of the Boom Clay pore network. These techniques were performed on freeze-dried samples without stress constraints at the initial state and after the tests.

The test protocol followed the one described in detail in Gonzalez-Blanco and Romero (2022), but as previously indicated, some additional stages were included to evaluate the self-sealing capacity. The main stages were the following:

(i) Pre-conditioning stage. Initially, an undrained loading stage at constant water content was set to reduce the suction induced due to the sampling retrieval at the HADES depth and to reproduce the in situ stress state of the clay. Total vertical stress was increased up to $\sigma_v = 3$ MPa at a 15 kPa/min rate. Then, the samples were put in contact with synthetic Boom Clay water (De Craen et al. 2004) (from now on referred to as water) at atmospheric pressure to minimise expansion on suction reduction (Sultan et al. 2010; Lima 2011; Bésuelle et al. 2014). Afterwards, upstream and downstream water pressures were increased to 0.6 and 0.5 MPa, respectively, and the water permeability was determined at steady-state under a pressure difference of 0.1 MPa. Subsequently, upstream water pressure was reduced to 0.5 MPa, followed by a time of pore pressure equalisation.

(ii) Loading stage. The samples were loaded within the elastic regime from $\sigma_v = 3$ MPa up to 6 MPa under drained conditions at a constant rate of 0.5 kPa/min while keeping a back-pressure of 0.5 MPa and ensuring not generating pore water pressure excess. To check the rate, the loading was stopped at specific intervals, recording the deformation with time, which was negligible.

(iii) Water permeability. At constant total vertical stress of 6 MPa, water permeability was measured again by applying a pressure difference of 0.1 MPa by increasing the upstream pressure to 0.6 MPa (downstream pressure was constant during the process). Afterwards, upstream water pressure was reduced to

0.5 MPa followed by a time of pore pressure equalisation.

(iv) Gas injection/dissipation. Initially, the water at the bottom line was rapidly replaced by gas at 0.5 MPa of initial pressure at the upstream boundary. Immediately after, gas injection started at a constant controlled volume rate of 100 mL/min until the gas pressure reached 4 MPa when the injection piston stopped (shut-off). Then, gas pressure was let to decay at constant gas volume. During this stage, the downstream line was full of a known volume of water at constant pressure (0.5 MPa).

(v) Re-saturation stage. After the gas dissipation, a re-saturation stage was performed. First, the sample was put in contact with water under atmospheric conditions at both upstream and downstream boundaries. When equilibrium was reached, water pressures were increased to 0.6 and 0.5 to measure the water permeability. Afterwards, upstream water pressure was reduced to 0.5 MPa followed by a time of pore pressure equalisation.

(vi) Unloading stage. Finally, the samples were unloaded under undrained conditions to preserve the microstructure thanks to the development of matric suction in the sample.

(vii) Microstructural study. MIP and μ-CT tests were performed on post-mortem samples.

This protocol was employed in two samples trimmed with the bedding planes parallel (S1_P) and normal (S2_N) to the flow direction. A third sample S3_N was subjected to a second gas injection to evaluate the possible fissure reactivation after self-sealing. The same procedure explained in (iv) was used for the second injection. Afterwards, stages (vi) and (vii) were carried out.

3 Experimental Results

3.1 Compressibility Behaviour

Figure 2 shows the continuous loading results at a controlled stress rate in terms of axial strain (positive in compression) and total vertical stress for samples tested with bedding planes normal (green lines, square symbols) and parallel (blue lines, round symbols) to the loading axis during stage (i). The figure also shows a compilation of results from previous research (Gonzalez-Blanco and Romero 2022). This compressibility is due to matric suction and stress changes. Samples tested with bedding planes parallel to the axis of revolution presented higher stiffness. This behaviour was attributed to the anisotropy in the elastic regime besides a possible closure of the discontinuities and/or bedding planes.

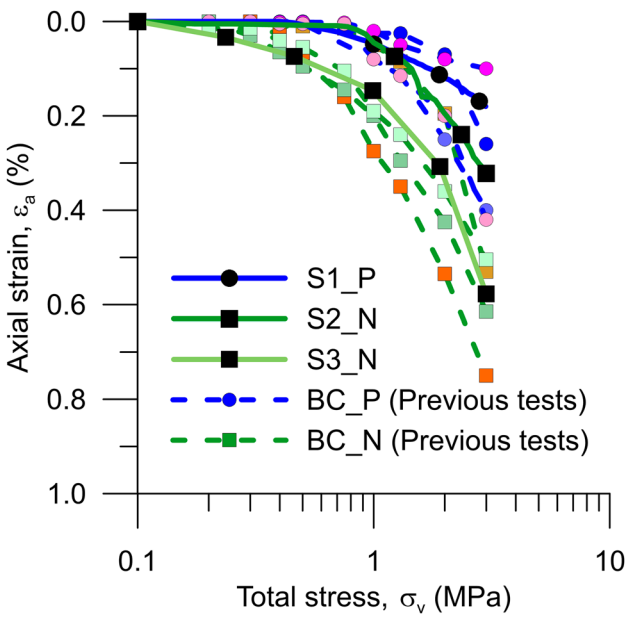

Fig. 2 Axial strain against total stress during fast loading at constant water content of samples at both orientations

Samples of Core 8 used in this study presented a higher stiffness than the ones used in previous campaigns, possibly due to the slight loss of water content during storage (Table 1).

Once total stress of 3 MPa was reached, the samples were put in contact with SBCW at atmospheric pressure at the top and bottom sides to ensure null matric suction. All samples underwent some swelling during this process. The expansion was lower in samples with bedding planes parallel to the axis, which were constrained to expand by oedometer conditions. The swelling was caused by some remaining matric suction. A small matric suction of 0.15 MPa was measured in an additional test and computed in a hydro-mechanical simulation (Gonzalez-Blanco et al. 2016). Figure 3 presents the swelling deformation of the samples during the flooding until its stabilisation with time (negative values correspond to expansion) together with previous results (Gonzalez-Blanco and Romero 2022).

At null matric suction of the samples, a continuous loading was carried out in all the oedometer tests at a slow stress rate of 0.5 kPa/min to ensure drained conditions. This rate allowed water to be expelled during the process. Consequently, there is no excess pore water pressure, and the deformation can be plotted in terms of effective vertical stress computed as the total stress minus the pore water pressure. Figure 4 shows the compressibility curves for samples with bedding planes normal and parallel to the axis together with previous results (Gonzalez-Blanco and Romero 2022). Despite being natural samples, good consistency was achieved during this hydro-mechanical loading. Small anisotropy behaviour during this stage was

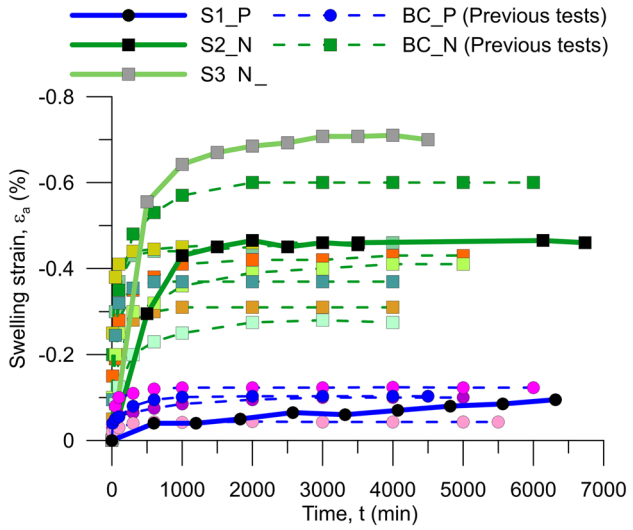

Fig. 3 Swelling strains during soaking at constant total stress of samples at both orientations

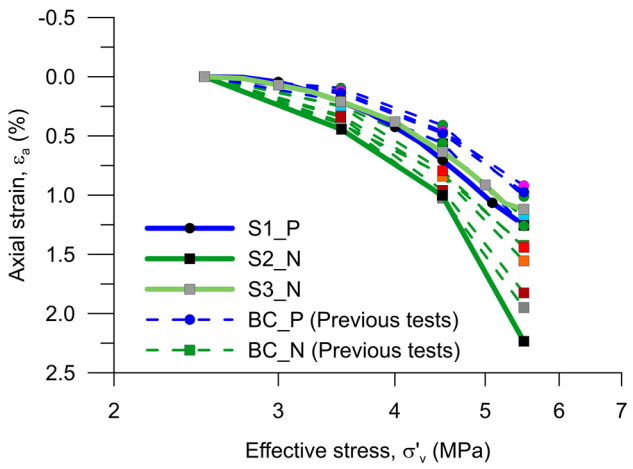

Fig. 4 Compressibility curves after saturation under continuous loading at drained conditions for samples at both orientations

identified, since samples with bedding planes normal to the axis still presented slightly higher compressibility.

3.2 Water Permeability Before Gas Injection

Figure 5 shows the water permeability as a function of the average void ratio for each sample. The results, in good concordance with the previous (lighter marks in the figure) (Gonzalez-Blanco and Romero 2022), highlighted the clear dependence of the water permeability on the porosity. Furthermore, as expected, higher water permeability was observed with flow parallel to bedding planes, indicating a marked anisotropic feature.

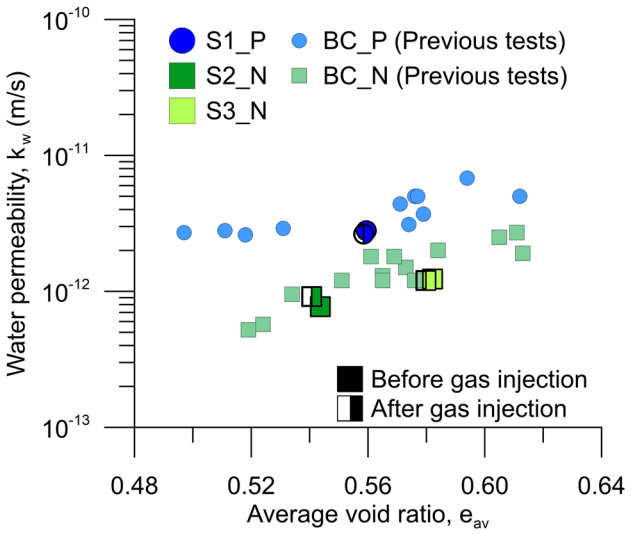

Fig. 5 Water permeability results as a function of the void ratio

3.3 Gas Injection and Dissipation

The gas injection was performed at a relatively large injection rate of 100 mL/min and with air, aiming to compare the macro-phenomenological behaviour and microstructural changes of the tested samples with the ones reported in Gonzalez-Blanco and Romero (2022). The injection pressure was increased until a maximum of 4 MPa (shut-off), and then, the injection system was stopped, while the total vertical stress was kept constant during the whole process (6 MPa). Gas passage through the samples was detected by a decrease in the inlet pressure and an increase in the outflow volume in the downstream PVC. This protocol differs from the typically called 'breakthrough tests' (Volckaert et al. 1995; Harrington and Horseman 1999; Rodwell 2000; Hildenbrand et al. 2004; Harrington et al. 2012; Wiseall et al. 2015; Liu et al. 2016a, b), in which gas pressure is constantly increased until some outflow volume is recorded indicating the breakthrough pressure. Moreover, gas flow through the ring–sample interface was discarded, since the maximum gas pressure was limited and consistently lower than the lateral stress measured in complementary tests (Gonzalez-Blanco and Romero 2022).

Figures 6 and 7 show the time evolution of the air inflow pressure at the upstream boundary, the outflow volume (at a constant downstream water pressure of 0.5 MPa), as well as the axial strain along gas injection and dissipation. The figures also present the previous tests (Gonzalez-Blanco and Romero 2022) of samples at both orientations. The gas pressure at the upstream boundary increased from 0.5 to 4 MPa in all cases ('A' to 'B' in the figures), followed by the shut-off (point 'B') and dissipation at constant inflow volume.

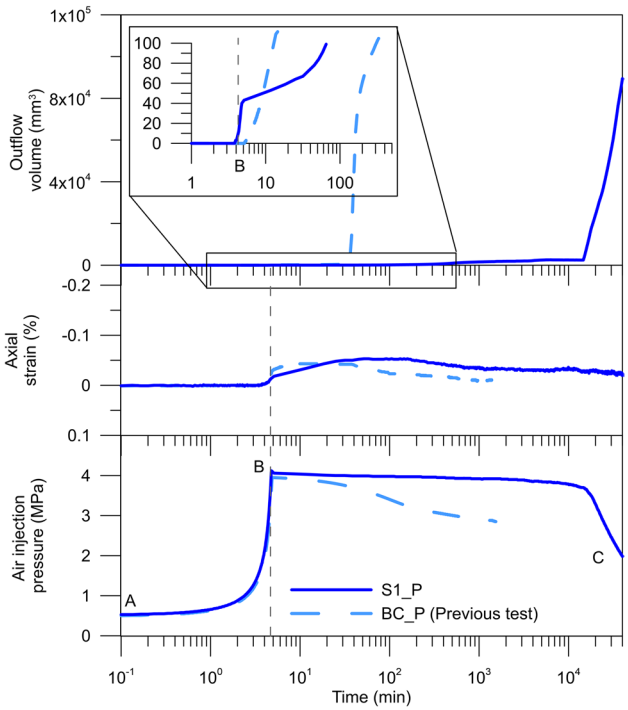

Fig. 6 Time evolution of the recorded data during gas injection/dissipation stage for samples with bedding planes parallel to flow: air injection pressure (bottom); axial strain computed from the vertical displacement (middle); outflow volume (top). Zoomed area in the upper graph from 1 to 500 min to observe the initial outflow volume

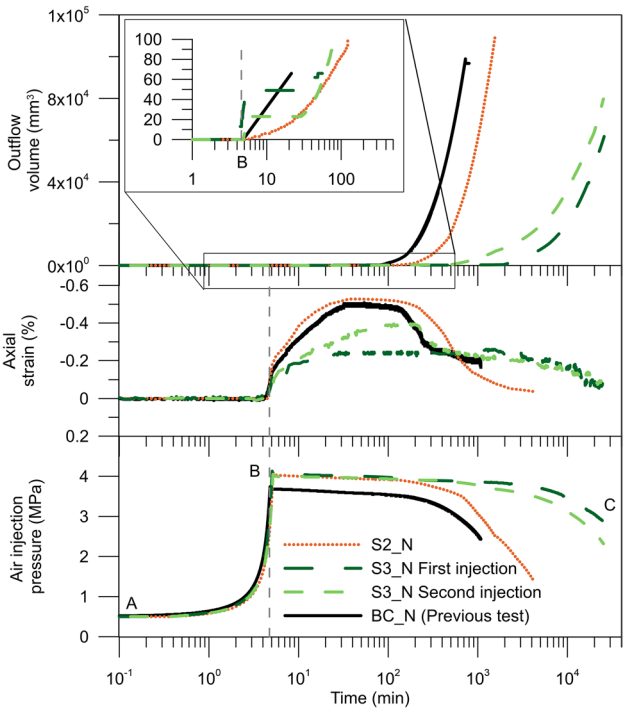

Fig. 7 Time evolution of the recorded data during gas injection/dissipation stage for samples with bedding planes normal to flow: air injection pressure (bottom); axial strain computed from the vertical displacement (middle); outflow volume (top). Zoomed area in the upper graph from 1 to 500 min to observe the initial outflow volume

A common behaviour was found in all the tests: while gas pressure increased, effective stress decreased, and samples underwent some expansion until the outflow took place; at such time, upstream pressure decreased, which implied an increase in effective stress and thus, samples displayed compression. Gas migration is, therefore, a highly coupled process.

These results reflected the trends already observed in the previous tests. Samples with bedding orientated normal to flow systematically showed larger expansion. This behaviour followed the anisotropic deformation detected on loading and soaking, since the samples with the bedding planes parallel to the flow are more constrained to expand due to the oedometer restriction. At that fast injection rate, it is observed a delay in response to the gas pressure front propagation, because samples underwent most of the expansion after the shut-off. The first outflow was detected during the dissipation stage, and the outflow volume rapidly increased, indicating the breakthrough time. The results are generally consistent with the previous ones, even though the tested samples belonged to different boreholes.

The outflow volume collected during gas dissipation was analysed to discern between the gas and the water volumes through two different procedures, since the initial amount of pressurised water in the outflow line (tubes and PVC's piston) was known. The volume of gas was initially estimated by pressurising the fluids in the closed outflow line using the perfect gas law. Afterwards, the volume of water was calculated by emptying the outflow line and comparing the initial and final volumes. These procedures can be affected by the dead volumes of the outflow line, although a rigorous calibration was performed. For all the tests, the volume of displaced water represented a marginal part of the total outflow, only around 1%. It implies that the global degree of saturation after the injection stage was still close to 1.

The expansion during gas pressurisation and the very slight desaturation observed during the gas injection/dissipation stage indicated that the primary transport mechanism is the gas flow through pressure-dilatant preferential pathways. Diffusion of dissolved gas through the pore water was disregarded, since the process was fast, and the diffusion coefficients reported for Boom Clay, both measured (Jacops et al. 2013, 2015) and numerically computed (Gonzalez-Blanco et al. 2016), are low. The preferential gas path development was confirmed by the analysis of the microstructure evolution (Gonzalez-Blanco and Romero 2022).

3.4 Re-saturation and Water Permeability

After the gas injection and dissipation stage, the samples were put in contact with water under atmospheric pressure until reaching steady-state conditions. During this stage, the deformation was very small (less than 0.05%), confirming that no significant desaturation occurred during the gas transport.

After stabilisation, water permeability was measured again by applying a hydraulic gradient at constant vertical stress (downstream and upstream water pressures were increased up to 0.6 MPa and 0.5 MPa, respectively). Figure 5 shows the results of this stage in comparison with the results obtained before the gas injection. For each sample, the water permeability values did not present significant changes, which might entail an excellent self-sealing of the fissures that formed during gas injection due to the re-saturation process. As the re-saturation was done under constant vertical stress, the driving mechanism of self-sealing is the swelling of clay minerals, although some creep could also contribute to the closure of the fissures. From these results, it can be concluded that Boom Clay's self-sealing capacity is significant in recovering the hydraulic barrier function.

3.5 Second Gas Injection

To study the possible fissure reactivation after self-sealing, a second gas injection stage was conducted on sample S3_N once it was re-saturated. The recorded data are shown in Fig. 7. Despite the similar behaviour, it can be noticed that for this second injection stage, the pressure dissipation was faster and the expansion larger. Moreover, although the time at which the first outflow occurred was equivalent, in the second, the outflow rate was more rapid, meaning that the gas flow entailed less restriction along the sample, suggesting the reopening of some preferential paths formed during the first injection, even if sealed during the re-saturation, still not completely healed. The microstructural analyses will support this hypothesis.

3.6 Gas Permeability

The gas permeability was computed under steady-state conditions during the dissipation stage, although gas flow was predicted to occur along localised pathways, for determining a global gas permeability (k_a), the entire area of the sample was taken into account. The pressure decay method (Arnedo et al. 2013; Pineda et al. 2014) and the generalised Darcy's law for compressible fluids were adopted. The recorded evolution of the absolute pressure decay ($\mathrm{d}\overline{u}_a/\mathrm{d}t$) from 4.1 MPa to around 2.1 MPa allowed estimating the mass of gas assuming perfect gas law at constant volume of the upstream reservoir (V) and constant downstream pressure at the top cap ($\overline{u}_{at}$):

$$k_a = \frac{k_i k_r \rho_a g}{\mu_a} = -\frac{2LV\rho_a g}{A\left(\overline{u}_a^{\,2} - \overline{u}_{at}^{\,2}\right)}\frac{\mathrm{d}\overline{u}_a}{\mathrm{d}t} \tag{1}$$

$$k_i k_r = -\frac{2\mu_a LV}{A\left(\overline{u}_a^{\,2} - \overline{u}_{at}^{\,2}\right)}\frac{\mathrm{d}\overline{u}_a}{\mathrm{d}t} \tag{2}$$

where k_i is the intrinsic permeability, k_r the relative permeability to air ($k_i k_r$ represents the effective permeability to air, independent of fluid properties, as a measure of the ability of this phase to flow in the presence of water), A and L are the cross-sectional area and length of the sample, μ_a the air dynamic viscosity at standard temperature and pressure, ρ_a the air density at standard temperature and pressure, and g the acceleration of gravity. $k_i k_r$ was used, since the degree of saturation of the material was not precisely known during the steady-state dissipation stage.

Effective air permeability is compared with intrinsic water permeability (measured in fully saturated conditions before and after the injection stage) in Fig. 8 as a function of the void ratio for the two bedding orientations. Three facts can be clearly discerned by observing the figure: (1) the air permeability is repeatedly higher than water permeability no matter the bedding orientation; (2) there is a clear anisotropy effect in the case of the water permeability (Fig. 5) that is not reproduced when gas flow is established;

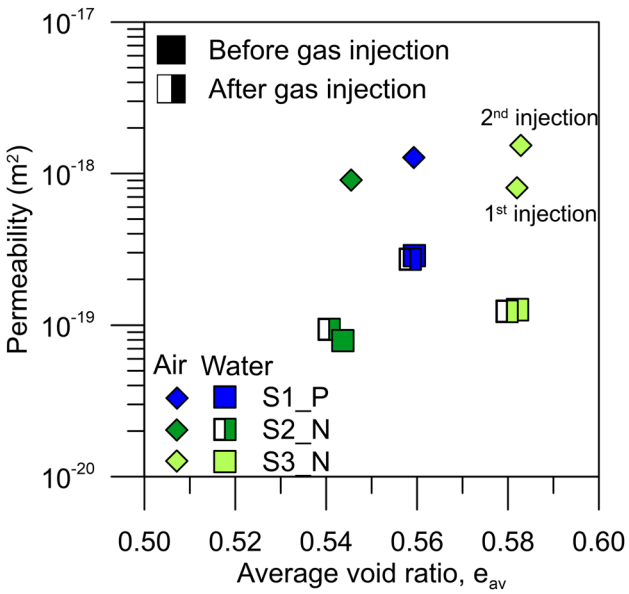

Fig. 8 Permeability to water and air against void ratio

and (3) the subsequent gas injection slightly increased the gas permeability. The two first points are consistent with those reported in Gonzalez-Blanco and Romero (2022). Therefore, gas flows through the fissures generated on gas injection, increasing the permeability for both orientations, as confirmed by the microstructure analyses in the next section.

3.7 Microstructural Analyses

The microstructure of the samples was studied using MIP and µ-CT and the results are compared with those reported in Gonzalez-Blanco and Romero (2022) for the initial state and after the gas injection tests. Representative sub-samples were carefully trimmed from oedometer specimens after the tests under unstressed conditions. Two different shapes were considered: a cubical shape of 1000 mm^3 for MIP and a cylindrical shape of 10 mm in height and 10 mm in diameter for µ-CT tests to avoid corner artefacts. In both cases, samples were subjected to a freeze-drying process, which is necessary for MIP, to allow comparison of the results.

The pore size density curves (PSDs) obtained with MIP for the intact state showed a monomodal distribution with a dominant size of 70 nm and low volume at the macro-scale. In contrast, samples after the gas injection tests performed in previous research campaigns (Gonzalez-Blanco et al. 2017; Gonzalez-Blanco and Romero 2022) consistently showed a new family of large pores. These new pore sizes larger than 2 µm were associated with the expansion undergone by Boom Clay samples during the gas injection and early shut-off stages and the dilation of gas pathways. These PSDs are now compared with the PSDs obtained after the re-saturation (S1_P and S2_N) and after the second gas injection stage (S3_N). Figure 9 shows that the PSDs curves in a log–log plane to emphasise the larger pore sizes. After re-saturation, lower volumes at the macro-scale than those for samples after gas injection are observed for both bedding orientations, nonetheless, these volumes are still slightly higher than the one corresponding to the intact sample, suggesting that there is no complete healing of the material during re-saturation and some pores or fissures did not completely close. On the other hand, the PSD of the sample after the second gas injection reveals the highest volume at the macro-scale. The analysis of the µ-CT images allows a better understanding of these results.

µ-CTs were performed on cylindrical samples using 720 projections on 360° with a voxel size of 20 µm. In samples S1_P and S2_N, one scanner was performed by trimming the sub-samples, so that the bedding planes were in the cross section of the cylinder, while for sample S3_N, two sub-samples were trimmed at different orientations to visualise the fissures that might develop due to gas passage in between the bedding planes. A sketch is shown for each sub-sampling

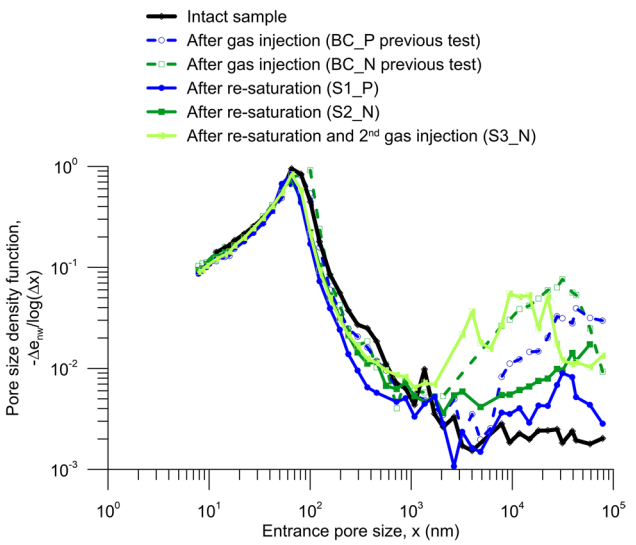

Fig. 9 Pore size density curves from MIP on the intact sample, samples after gas injection tests, samples after re-saturation and sample after second gas injection

orientation in Figs. 10 and 11. Besides, the figures present the cross-sectional images at the mid-plane and the 3D volume reconstructed using ImageJ software (Schneider et al. 2012).

As can be observed in Fig. 10, large-aperture fissures (larger than 40 µm, which is double the scanner resolution) were not identified by the µ-CT in either orientation after the re-saturation process, although they were systematically detected after the gas injection tests of the previous research (Gonzalez-Blanco and Romero 2022). This fact suggests an excellent self-sealing of the fissures formed during the gas injection. However, it was detected the presence of some large pores in both orientations that were not observed previously. They are associated with some gas entrapped in macro-pores that were not completely closed during the re-saturation and were magnified on undrained unloading. These pores are encircled in the cross-sectional images (Fig. 10b) and isolated in Fig. 10d after a segmentation process. Nonetheless, at the current resolution, they did not present connectivity, which is consistent with the recovery of the initial water permeability after the re-saturation. On the contrary, large-aperture fissures acting as gas pathways were detected on the sample after the second injection stage (Fig. 10 at the bottom), together with some large pores probably caused by some gas entrapment during the first injection. In that arrangement, the fissures coincided with the direction of the bedding planes, as reported by Gonzalez-Blanco and Romero (2022). However, to establish a flow normal to the bedding, it is required the development of some low-aperture fissures bridging the bedding planes, which cannot be identified in the images in Fig. 10. To try

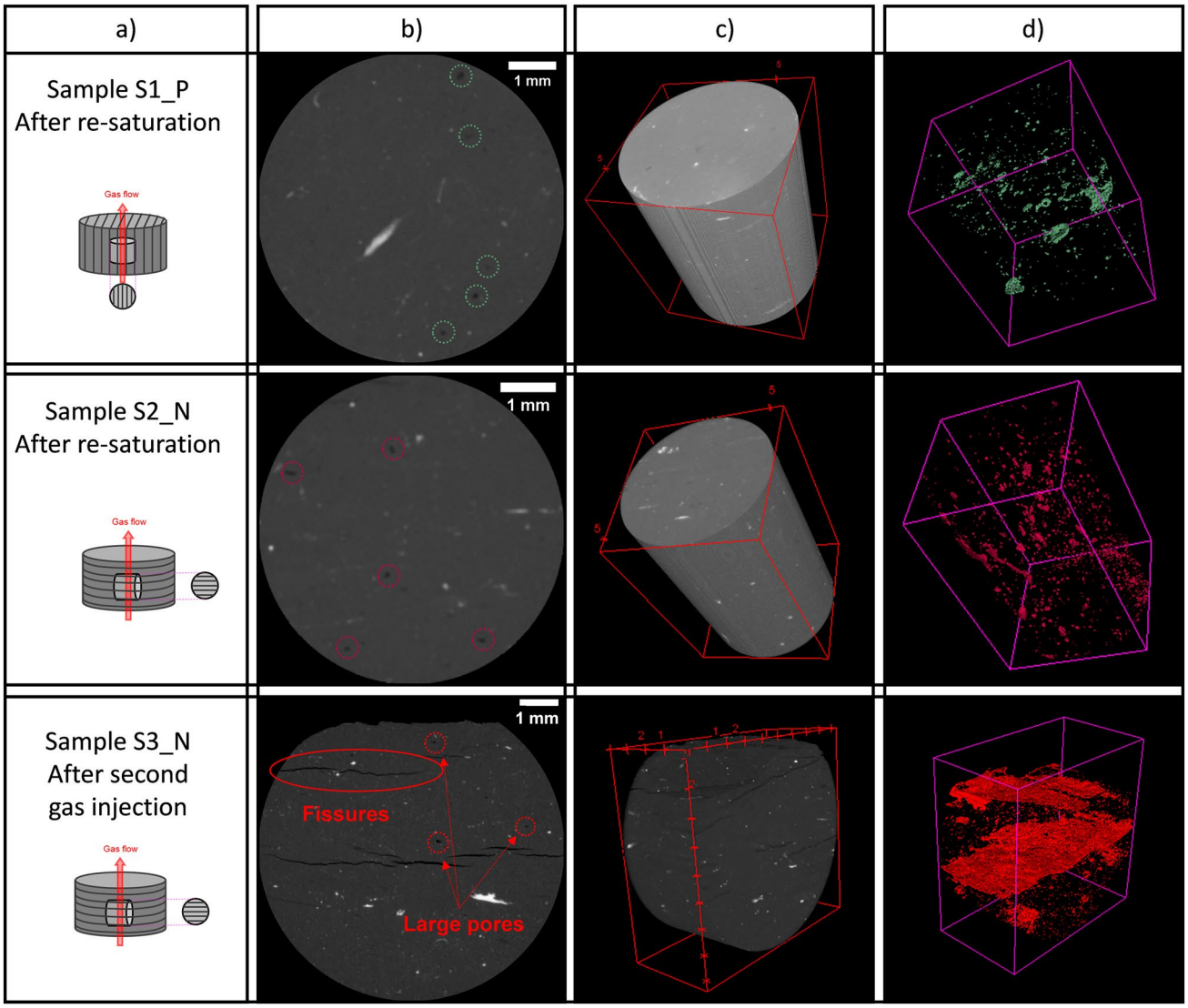

Fig. 10 **a** Sub-sampling scheme; **b** cross section at the mid-height; **c** 3D volume reconstruction of μ-CT images; and **d** porosity segmentation of the samples S1_P after re-saturation (top) and S2_N after re-saturation (middle) and S3_N after second gas injection (bottom)

to detect them, sample S3_N was also trimmed with the beddings orthogonal to the axis of revolution, as indicated in Fig. 11d. With the sub-sample in this position and improving the scanner resolution to 10 μm, it is possible to discern some of these low-aperture fissures, which are unconnected due to their closure during the gas dissipation (compression of the sample in the last stage). Nonetheless, only a few fissures with apertures between 20 and 40 μm were detected oblique to the bedding planes (Fig. 11). Therefore, the majority of these fissures connecting bedding planes should have apertures between 2 and 20 μm, which are detected in the PSD curves determined by MIP.

To have a broad view that facilitates the comprehension of microstructural evolution due to the different processes, Fig. 12 compares the μ-CT images for samples with bedding planes parallel and normal to the flow at the initial state, after gas injection and after re-saturation. It also includes the image of the sample with the bedding planes normal to the flow after a second injection. For the intact state, a very small volume of pores can be identified and bedding planes are not visible at the current resolution. After the gas injection, samples at both orientations present fissures in the direction of the bedding planes. The analysis of the fissure network (Gonzalez-Blanco and Romero 2022) showed that on the sample with bedding planes parallel to flow, the fissures are closer and have lower mean aperture than in the opposite orientation. This is because the radial deformation was restricted by the oedometer conditions. However, the fissure density was remarkably similar for both orientations, which points out

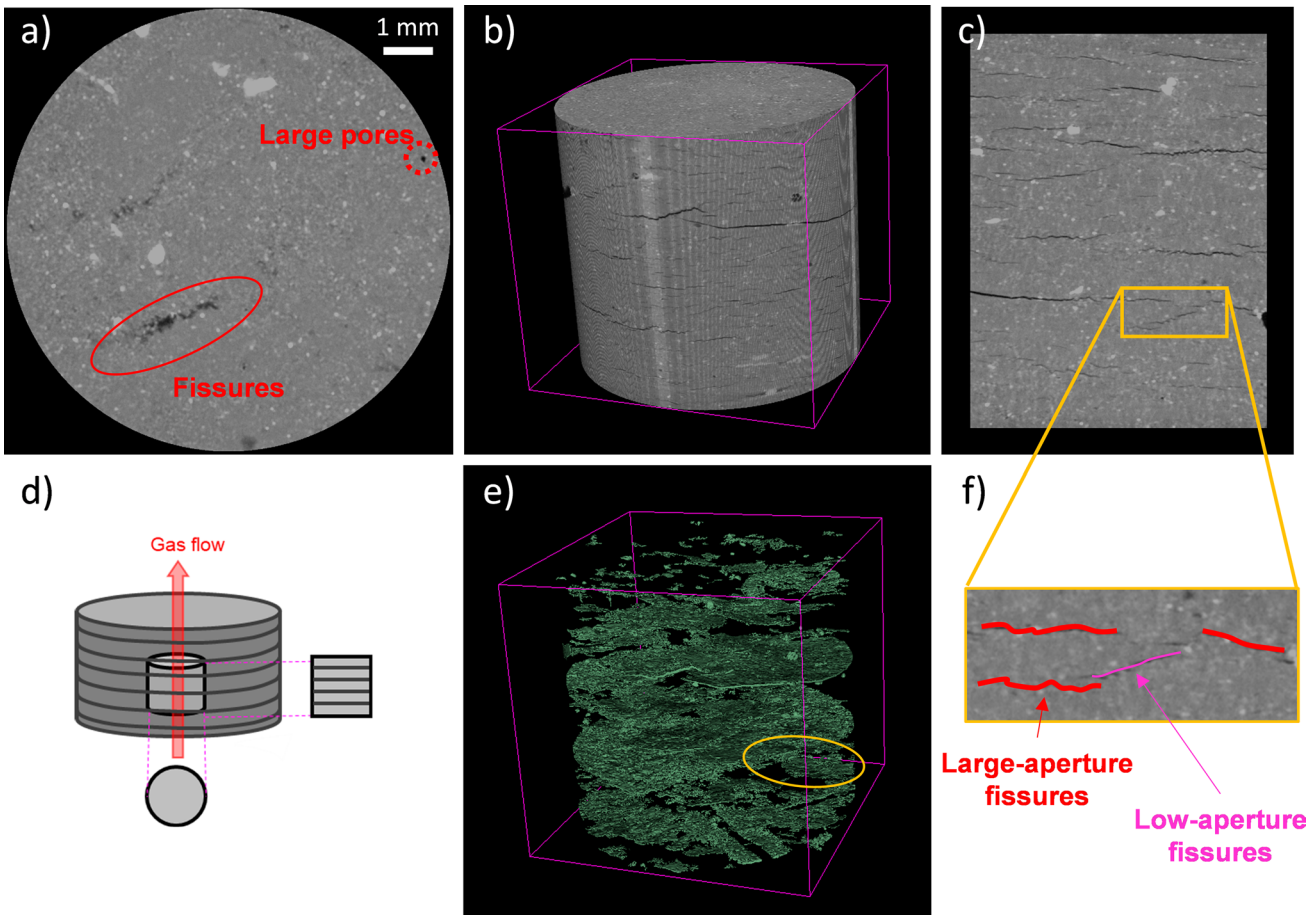

Fig. 11 μ-CT data of sample S3_N after second gas injection with improved resolution. **a** Cross section at the mid-height; **b** 3D volume reconstruction of μ-CT images; **c** longitudinal section at the middle; **d** sub-sampling scheme; **e** porosity segmentation and **f** zoom showing a low-aperture fissure bridging large-aperture fissures

that there are not significant orientation effects during gas transport, which is consistent with the results regarding effective gas permeability that did not present anisotropy. After the re-saturation, the fissures self-sealed on both orientations, but as previously mentioned, some large pores remained after this process. Again, the volume detected is quantitatively similar for both orientations.

In the case of the sample subjected to a second injection, the mean aperture of the fissures is slightly higher than after the first gas injection, again consistent with the higher gas permeability. This is a consequence of some memory of the fissure network developed during the gas injection, which entailed mechanical damage to the material. In addition, the pores with entrapped gas could form due to an ununiformed closure of the pathways during the re-saturation. Nonetheless, it is worth noticing that the microstructural analyses were performed after an undrained loading, and consequently, these air-filled macro-pores could be enlarged during this path, as the volume of entrapped gas under stress conditions was not so significant.

4 Discussion of the Results Within a Multi-scale Insight

The changes in permeability are clearly linked to the evolution of the microstructure in Boom Clay. In the previous research (Gonzalez-Blanco and Romero 2022), the intrinsic permeability and air-entry value were related to the microstructure by an approach based on the fissured volume. The volume was associated with the progressive degradation undergone by the material during fissure generation and growth. To this aim, a fissured void ratio e_f —volume of fissures to the volume of solids—was defined as the area below the *PSD* curves obtained by MIP after the gas tests for pore sizes larger than 2 μm. The volume of fissures to the volume of voids—fissure fraction e_f/e —was also determined. Then, a damage variable D was

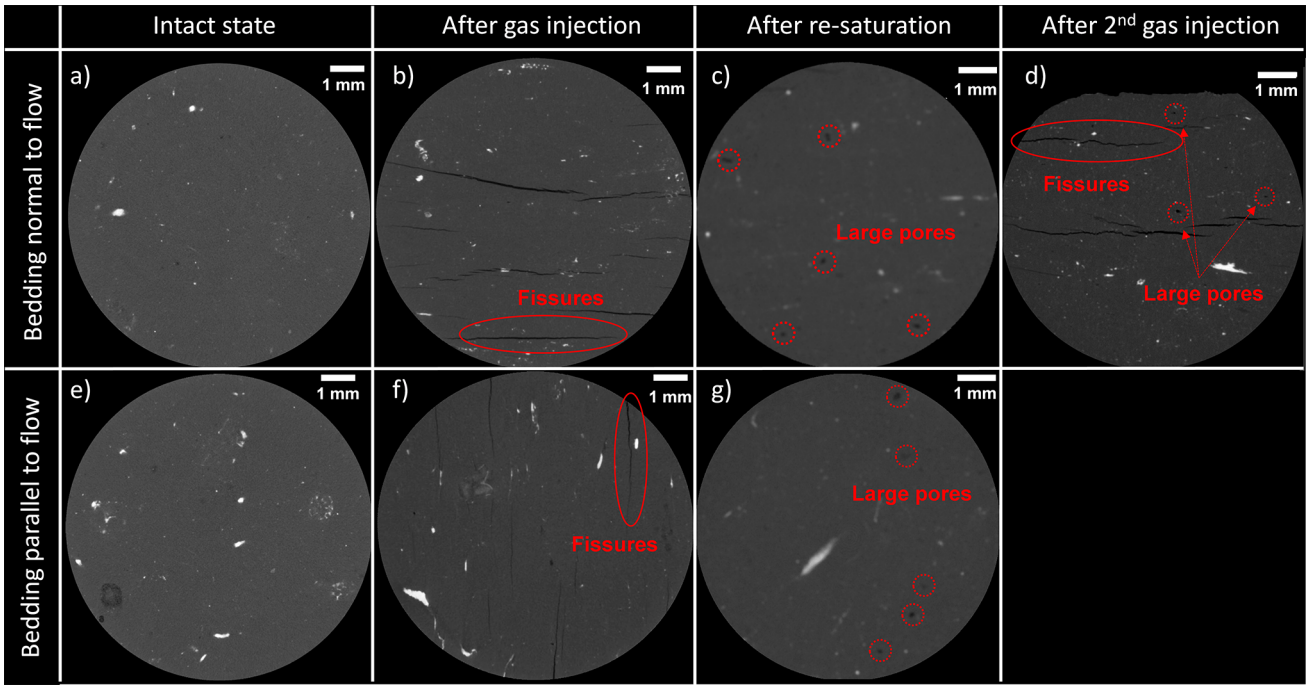

Fig. 12 Cross-sectional μ-CT images of Boom Clay samples. Top: sample with bedding planes normal to flow **a** at the intact state (Gonzalez-Blanco and Romero 2022); **b** after gas injection (Gonzalez-Blanco and Romero 2022); **c** after re-saturation; **d** after second gas injection. Bottom: sample with bedding planes parallel to flow: **e** at the intact state (Gonzalez-Blanco and Romero 2022); **f** after gas injection (Gonzalez-Blanco and Romero 2022); **g** after re-saturation

introduced based on this fissured fraction (ratio of the fissured fraction to the maximum fissured fraction), which affected the macroscopic gas transport properties, air-entry value and intrinsic permeability.

For these new results, a similar approach is used. Nonetheless, the fissured fraction has been redefined to include the large pores detected after the re-saturation (Fig. 10). Consequently, the total void ratio is defined as the sum of the volume of the micro-pores (V_m), the volume of the macro-pores (V_M) and the volume of fissures (V_f) to the volume of solids (V_s):

$$e = \frac{V_m + V_M + V_f}{V_s} \tag{3}$$

To account for these volumes, a macro-fissured ratio is defined as

$$f = \frac{e_f + e_M}{e} \tag{4}$$

where e_f is the fissured void ratio (V_f/V_s) and e_M is the macro void ratio (V_M/V_s). Here, the total void ratio e represents the final state when the MIP is performed and e_M and e_f are computed. The total void ratio is incorporated in the fraction, because its variation during the injection and re-saturation stages is relatively small.

The volumes to define f are calculated first from μ-CT images after the filtering process. Figure 10 shows a 3D view of the macro-pores for the two samples after the re-saturation tests (S1_P and S2_N). For sample S3_N, which was subjected to a second injection after re-saturation, the filtering includes both the fissures generated during the second gas injection and some pores that might be related to the first injection and not sealed during the re-saturation. The obtained values for each of the samples are gathered in Table 2.

Values of e_f and e_M from MIP data were determined by calculating the area below the *PSD* curves after the tests for

Table 2 Total volume of the sample, macro-pore volume and volume of the large-aperture fissures (μ-CT data)

Volumes	After re-saturation		After second gas injection
	S1_P	S2_N	S3_N
V_{total}(mm^3)	1238	962	290
V_M(mm^3)	8.77	11.73	6.25
V_f(mm^3)	0	0	
Percentage over the total volume (%)	0.7	1.2	2.2

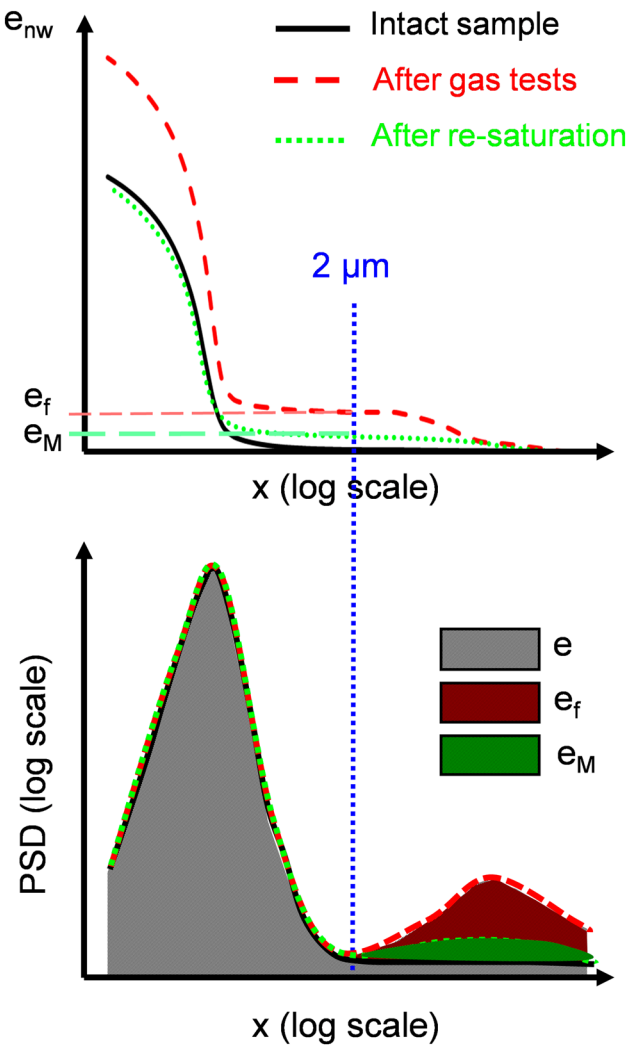

Fig. 13 Schematic used for calculating the macro void ratio and fissured void ratio using PSD curves from MIP

Table 3 Values of macro void ratio plus fissured void ratio and macro-fissured ratio using MIP and µ-CT data

Sample	Technique	$e_f + e_M$	f
S1_P	MIP (x >2 µm)	0.015	0.028
Bedding//flow (e=0.559)	MIP (x > 40 µm)	0.011	0.019
	µ-CT (x > 40 µm)	0.011	0.020
S2_N	MIP (x > 2 µm)	0.020	0.037
Bedding ⊥ flow (e=0.540)	MIP (x > 40 µm)	0.017	0.031
	µ-CT (x > 40 µm)	0.019	0.035
S3_N	MIP (x > 2 µm)	0.087	0.149
Bedding ⊥ flow (e=0.582)	MIP (x > 40 µm)	0.032	0.056
	µ-CT (x > 40 µm)	0.034	0.059

pore sizes x larger than 2 µm (Fig. 13). To compare them with µ-CT data, sizes larger than 40 µm are also considered. Table 3 presents the results showing a good consistency between the two techniques.

In the approach presented by Gonzalez-Blanco and Romero (2022), the water permeability of the intact (undamaged) state was considered unique regardless of the bedding orientation. An average value based on the different water permeability measurements under full saturation for each orientation was assumed (mean value of 2.4×10^{-19} m^2 for flow normal to bedding and 4.4×10^{-19} m^2 for flow parallel to bedding). Here, the self-sealing capacity due to the re-saturation has been accounted for by comparing the water permeability before and after the gas injection. Therefore, the water permeability cannot be considered an average value for the analyses, since its value obviously depends on the total void ratio and the orientation of the bedding planes. This fact becomes evident by observing the permeability to water and gas at the different stages of the tests, as indicated in Fig. 8. To consider the initial value of the water permeability, a permeability ratio is defined as k/k_{initial}, being k the permeability measured during the last stage of the tests (whether during gas or water flow) and normalised with the initial permeability to water before any injection. This approach is similar to the damage model reported in Fall et al. (2014), in which the permeability ratio is exponentially related to porosity.

The permeability ratio was then calculated for all tested samples [including the previous results of gas injection tests (Gonzalez-Blanco and Romero 2022)] to correlate it with the damage variable f. For its computation, MIP information was used, since it provides data of a wider range of pore sizes than µ-CT. The water permeability measured before the gas injection stage was taken as the value of k_{initial}. In this manner, a linear relationship can be established between the permeability ratio and the macro-fissured ratio:

$$\frac{k}{k_{\text{initial}}} = \left[\alpha_i (f - f_0) + 1\right] \tag{5}$$

where f_0 represents the volume of the macro-pores at the intact state, which is independent of the bedding orientation and can be obtained with MIP data. Considering pore sizes larger than 2 µm for the calculation, $f_0 = 0.02$. Conversely, the value of α_i is a constant parameter that depends on the orientation of the bedding concerning the flow and is fitted with the experimental data.

The proposed model (Fig. 14) can accurately represent: (1) the fissures developed during the gas injection, which induce an increase in effective permeability; (2) their closure during re-saturation, which implies the recovery of the initial permeability, including the unconnected macro-pores of occluded gas; and (3) the increase

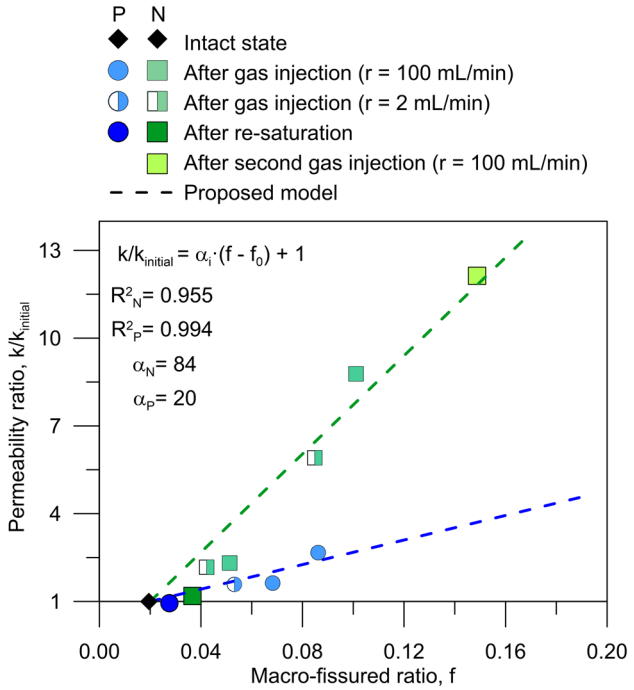

Fig. 14 Proposed linear model relating the macro-fissured ratio with the permeability ratio for both bedding orientations (P: samples with bedding planes parallel to flow; N: samples with bedding planes normal to flow)

in macro-fissure ratio when a successive injection is performed, reflecting both the development of fissures and macro-pores which leads to the highest gas permeability. However, it is necessary to fit the slope parameter for each orientation, since samples with bedding planes normal to the flow present a more significant increase in the permeability ratio for the same damage during the gas injection. A value of $\alpha_P = 20$ is obtained for samples with bedding planes parallel to flow, whereas $\alpha_N = 84$ for the opposite orientation. This is a consequence of the importance of the Boom Clay anisotropy and the effect of oedometer conditions. The initial permeability is higher in samples with bedding planes parallel to flow due to the favourable orientation of these initially closed discontinuities. For the gas flow, the opening of the bedding, together with the development of some bridging planes, is required. During this process, samples with the bedding normal to flow are less restricted to open because of the oedometer conditions, and in fact, present a higher expansion during the gas pressurisation and dissipation. Although gas permeability values are equivalent for both orientations, the increase in permeability compared to the initial one is larger for the samples with bedding planes normal to the flow and is accounted for in the model throughout a larger α parameter. After re-saturation and closure of the fissures, initial permeability is practically recovered for both orientations, resuming the initial anisotropy. Figure 15 compiles schematically the key parameters taking place in each of the processes. Despite the simplicity of the model, complex macroscopic hydro-mechanical behaviour, such as gas transport on initially saturated Boom Clay and its self-sealing capacity, can be described through the evolution of its microstructure.

5 Concluding Remarks

The ability to self-seal of the argillaceous rocks is a property that favours the hydraulic barrier function of radioactive waste disposal systems. This paper has presented experimental results dealing with the self-sealing capacity of Boom Clay, a potential host rock in Belgium, after gas transport. The effectiveness of the self-sealing was evaluated by comparing water permeability before and after the gas invasion. In addition, a test was performed to study the possible fissure reactivation during gas transport after self-sealing.

First, initial water permeability under oedometer conditions was determined for two sample bedding orientations, parallel and normal to the flow, showing a marked anisotropic behaviour. Samples with bedding planes orientated favourable to the flow (parallel) presented a higher initial water permeability. Then, the samples were subjected to a gas injection and dissipation stage at constant vertical stress. As a consequence of gas invasion, pressure-induced fissures developed. The fissure network was characterised using complementary microstructural techniques (MIP and µ-CT) in previous research work (Gonzalez-Blanco and Romero 2022). A family of new fissures larger than 2 µm were detected with MIP regardless of the bedding orientation. Images from µ-CT allowed identifying the large-aperture fissures in the direction of the bedding planes. As a result of the fissure development, effective gas permeability was larger than the initial one in all the tested samples and presented an isotropic response.

The re-saturation of the samples at constant vertical stress led to the recovery of the initial permeability for both orientations, replicating the original anisotropy, which was considered evidence of the good self-sealing capacity of Boom Clay. However, the complete self-healing was not conspicuous, since the microstructural analyses showed higher volumes at the macro-scale than in the initial state, possibly due to some gas entrapment or occlusion in large pores, which were not completely closed during the re-saturation. However, they did not present connectivity, in agreement with restoring the initial permeability.

In a further step, a second gas injection was performed in a sample with bedding planes normal to the flow after the re-saturation. The effective gas permeability measured in this case was the highest one in concordance with the largest

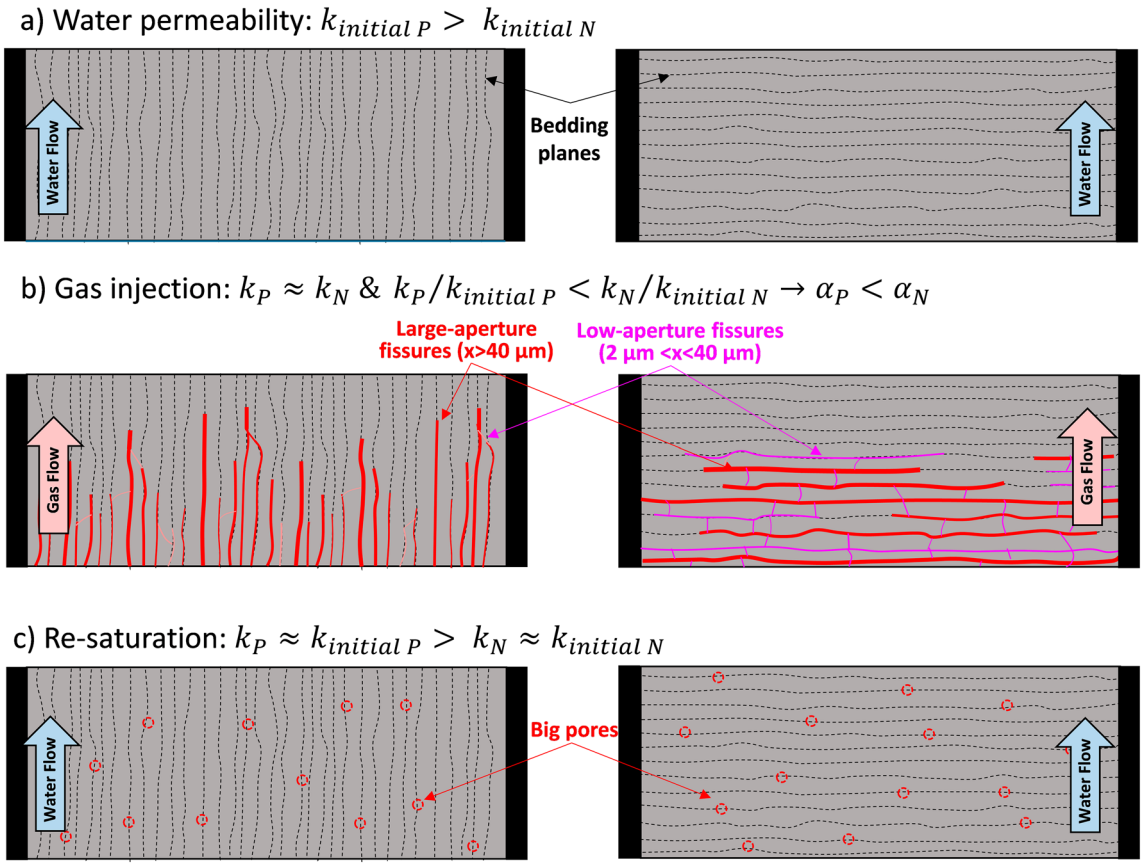

Fig. 15 Representation of fluid transport for each of the processes that the model described, key variables and parameters. Dashed lines indicate bedding planes, continuous lines represent gas pathways and circles are pores with entrapped gas

volume of pores at the macro-scale detected by MIP. µ-CT image analyses showed the opening of large-aperture fissures in the direction of the bedding planes and, improving the resolution, low-aperture fissures bridging the bedding planes were also identified. Moreover, some large pores were detected in the images, likely related to some gas entrapment during the first injection and enlarged on undrained unloading. These facts suggested that the second episode of gas invasion could reopen the fissures and permit the gas flow easily. However, more research is needed to confirm it (i.e., second injection at different bedding orientations).

At the end of the paper, a model was proposed to account for the permeability changes in terms of a microstructural damage variable. A macro-fissured void ratio was defined using MIP data to consider the pore network evolution of the Boom Clay from the initial condition to the state after each of the different transport processes. Despite its simplicity, the model can represent complex hydro-mechanical behaviour—gas injection and self-sealing—within a multi-scale perspective.

Acknowledgements This project has received funding from the European Union's Horizon 2020 research and innovation programme 'European Joint Programme on Radioactive Waste Management (EURAD)' (2019–2024) WP-Gas 'Mechanistic understanding of gas transport in clay materials' under Grant agreement No. 847593. In addition, the acknowledgements are extended to the Belgian Agency for Radioactive Waste and Enriched Fissile Materials (ONDRAF/NIRAS) for funding this research program under contract No. CCHO 2021-0377/00/00 (2021–2024).

Funding Open Access funding provided thanks to the CRUE-CSIC agreement with Springer Nature. This project has received funding from the European Union's Horizon 2020 research and innovation programme 'European Joint Programme on Radioactive Waste Management (EURAD)' (2019–2024) WP-Gas 'Mechanistic understanding of gas transport in clay materials' under Grant agreement No. 847593. Research contract CCHO 2021-0377/00/00 (2021–2024) with ONDRAF/NIRAS (Belgian Agency for Radioactive Waste and Enriched Fissile Materials) also provided funding.

Data Availability Experimental data are not provided in files. Relevant information is reported in figures and tables.

Code Availability Not applicable.

Declarations

Conflict of Interest The authors declare no conflict of interest.

References

Andra (2005) Evaluation of the feasibility of a geological repository in an argillaceous formation

Arnedo D, Alonso EE, Olivella S (2013) Gas flow in anisotropic claystone: modelling triaxial experiments. Int J Numer Anal Meth Geomech 37:2239–2256

Bastiaens W, Bernier F, Li XL (2007) SELFRAC: experiments and conclusions on fracturing, self-healing and self-sealing processes in clays. Phys Chem Earth 32(8–14):600–615

Bernier F, Li XL, Bastiaens W, Ortiz L, Van Geet M, Wouters L, Frieg B, Blümling P, Desrues J, Viaggiani G, Coll C, Chanchole S, De Greef V, Hamza R, Malinsky L, Vervoort A, Vanbrabant Y, Debecker B, Verstraelen J et al (2007a) Fractures and self-healing within the excavation disturbed zone in clays (SELFFRAC)

Bernier F, Li XL, Bastiaens W (2007b) Twenty-five years' geotechnical observation and testing in the Tertiary Boom Clay formation. Géotechnique 57(2):229–237

Bésuelle P, Viggiani G, Desrues J, Coll C, Charrier P (2014) A laboratory experimental study of the hydromechanical behavior of boom clay. Rock Mech Rock Eng 47(1):143–155

Cevatoglu M, Bull JM, Vardy ME, Gernon TM, Wright IC, Long D (2015) Gas migration pathways, controlling mechanisms and changes in sediment acoustic properties observed in a controlled sub-seabed CO2 release experiment. Int J Greenh Gas Control 38(2015):26–43. https://doi.org/10.1016/j.ijggc.2015.03.005

Cnudde V, Boone MN (2013) High-resolution X-ray computed tomography in geosciences: a review of the current technology and applications. Earth-Sci Rev 123(2013):1–17. https://doi.org/10.1016/j.earscirev.2013.04.003

Cuss R, Harrington J, Giot R, Auvray C (2014) Experimental observations of mechanical dilation at the onset of gas flow in Callovo-Oxfordian claystone. Geol Soc Lond Spec Publ 400:507–519

De Craen M, Wang L, Van Geet M, Moors H (2004) Geochemistry of boom clay pore water at the mol site

Delage P, Le TT, Tang AM, Cui YJ, Li XL (2007) Suction effects in deep Boom Clay block samples. Géotechnique 57(1):293–244

Di Donna A, Charrier P, Dijkstra J, Andò E, Bésuelle P (2022) The contribution of swelling to self-sealing of claystone studied through X-ray tomography. Phys Chem Earth 127:103191

EURAD (2019) EURAD Deployment plan 2019–2024. HORIZON 2020 project EURAD. EC Grant agreement no: 847593, p 25. https://www.ejp-eurad.eu/publications/eurad-deployment-plan

Fall M, Nasir O, Nguyen TS (2014) A coupled hydro-mechanical model for simulation of gas migration in host sedimentary rocks for nuclear waste repositories. Eng Geol 176:24–44

Gerard P, Harrington J, Charlier R, Collin F (2014) Modelling of localised gas preferential pathways in claystone. Int J Rock Mech Min Sci 67:104–114. https://doi.org/10.1016/j.ijrmms.2014.01.009

Giger SB, Marschall P, Lanyon GW, Derek Martin C (2015) Transferring the geomechanical behaviour of Opalinus Clay observed in lab tests and Mont Terri URL to assess engineering suitability at potential repository sites. In: 49th US rock mechanics/geomechanics symposium, San Francisco, CA, USA, 28 June–1 July, 2015

Giot R, Auvray C, Talandier J (2019) Self-sealing of claystone under X-ray nanotomography. Geol Soc Spec Pub 482(1):213–223

Gonzalez-Blanco L, Romero E (2022) A multi-scale insight into gas migration in a deep Cenozoic clay. Géotechnique. https://doi.org/10.1680/jgeot.21.00208

Gonzalez-Blanco L, Romero E, Jommi C, Li X, Sillen X (2016) Gas migration in a Cenozoic clay: experimental results and numerical modelling. Geomech Energy Environ 6:81–100

Gonzalez-Blanco L, Romero E, Jommi C, Sillen X, Li X (2017) Exploring fissure opening and their connectivity in a cenozoic clay during gas injection. In: Ferrari A, Laloui L (eds) Advances in laboratory testing and modelling of soils and shales (ATMSS). Springer series in geomechanics and geoengineering. Springer, Cham, pp 288–295. https://doi.org/10.1007/978-3-319-52773-4_33

Gonzalez-Blanco L, Romero E, Marschall P, Levasseur S (2022) Hydro-mechanical response to gas transfer of deep argillaceous host rocks for radioactive waste disposal. Rock Mech Rock Eng 55(3):1159–1177. https://doi.org/10.1007/s00603-021-02717-3

Harrington JF, Horseman ST (1999) Gas transport properties of clays and mudrocks. Geol Soc Lond Spec Publ 158(1):107–124. https://doi.org/10.1144/GSL.SP.1999.158.01.09

Harrington JF, de la Vaissière R, Noy DJ, Cuss RJ, Talandier J (2012) Gas flow in Callovo-Oxfordian claystone (COx): results from laboratory and field-scale measurements. Mineral Mag 76(8):3303–3318

Harrington JF, Cuss RJ, Talandier J (2017) Gas transport properties through intact and fractured Callovo-Oxfordian mudstones. Geol Soc Lond Spec Publ 454(1):131–154. https://doi.org/10.1144/SP454.7

Hildenbrand A, Schlömer S, Krooss BM, Littke R (2004) Gas breakthrough experiments on pelitic rocks: comparative study with N2, CO2 and CH4. Geofluids 4:61–80

Honty M, Maes N, Fürychova P (2017) Self-sealing of an alkaline plume affected Boom Clay evidenced by microCT and hydraulic conductivity measurements. *SCK·CEN/21686881*, (February), p 32. http://www.sckcen.be

Jacops E, Volckaert G, Maes N, Weetjens E, Govaerts J (2013) Determination of gas diffusion coefficients in saturated porous media: He and CH4 diffusion in Boom Clay. Appl Clay Sci 83–84:217–223

Jacops E, Wouters K, Volckaert G, Moors H, Maes N, Bruggeman C, Swennen R, Littke R (2015) Measuring the effective diffusion coefficient of dissolved hydrogen in saturated Boom Clay. Appl Geochem 61:175–184

Levasseur S, Collin F, Daniels K, Dymitrowska M, Harrington J, Jacops E, Kolditz O, Marschall P, Norris S, Sillen X, Talandier J, Truche L, Wendling J (2021) Initial state of the art on gas transport in clayey materials. Deliverable D6.1 of HORIZON 2020 project EURAD, Work Package Gas. EC Grant agreement no: 847593, p 384

Lima A (2011) Thermo-hydro-mechanical behaviour of two deep Belgian clay formations: Boom and Ypresian clays. PhD Thesis, Universitat Politècnica de Catalunya, Barcelona, Spain

Liu JF, Song Y, Skoczylas F, Liu J (2016a) Gas migration through water-saturated bentonite–sand mixtures, COx argillite, and their interfaces. Can Geotech J 53(1):60–71

Liu ZB, Shao JF, Liu TG, Xie SY, Conil N (2016b) Gas permeability evolution mechanism during creep of a low permeable claystone. Appl Clay Sci 129(July):47–53

Nagra (2002) Technical Report 02-23. Opalinus Clay Project. FEP Management for Safety Assessment

NEA (2010) Annual report

ONDRAF/NIRAS (2013) Research, Development and Demonstration (RD&D) Plan for the geological disposal of high-level and/or long-lived radioactive waste including irradiated fuel if considered as waste. State-of-the-art report as of December 2012

Paul S, Roy S, Ghosh P, Faghihi Zarandi MA, Cender T, Pillai KM (2019) A novel method for permeability estimation from micro-tomographic images. Transp Porous Media 127(1):171–190. https://doi.org/10.1007/s11242-018-1186-z

Pineda J, Romero E, Alonso EE, Pérez T (2014) A new high-pressure triaxial apparatus for inducing and tracking hydro-mechanical degradation of clayey rocks. Geotech Test J 37(6):1–15

Rodwell WR (editor) (2000) Research into gas generation and migration in radioactive waste repository systems (PROGRESS Project). c:%5CCIEMAT%5CBIBLIOGRAF?A%5CRodwell_2000_ResearchIntoGas.pdf.

Romero E, Simms PH (2008) Microstructure investigation in unsaturated soils: a review with special attention to contribution of Mercury Intrusion Porosimetry and Environmental Scanning Electron Microscopy. Geotech Geol Eng 26:705–727

Salehnia F, Collin F, Li XL, Dizier A, Sillen X, Charlier R (2015) Coupled modeling of excavation damaged zone in Boom clay: strain localization in rock and distribution of contact pressure on the gallery's lining. Comput Geotech 69:396–410

Schneider CA, Rasband WS, Eliceiri KW (2016) NIH Image to ImageJ: 25 years of image analysis. Nat Methods 9(7):671–675

Senger R, Romero E, Marschall P (2018) Modeling of gas migration through low-permeability clay rock using information on pressure and deformation from fast air injection tests. Transp Porous Media 123(3):563–579. https://doi.org/10.1007/s11242-017-0962-5

Sultan N, Cui Y-J, Delage P (2010) Yielding and plastic behaviour of Boom clay. Géotechnique 60(9):657–666

Van Geet M, Bastiaens W, Ortiz L (2008) Self-sealing capacity of argillaceous rocks: review of laboratory results obtained from the SELFRAC project. Phys Chem Earth 33(Supplement 1):S396–S406. https://doi.org/10.1016/j.pce.2008.10.063

Volckaert G, Ortiz L, De Canniere P, Put M, Horseman ST, Harrington JF, Fioravante V, Impey M (1995) MEGAS Modelling and experiments on gas migration in repository host rocks

Volckaert G, Mallants D, Bush R, Lambers L (1998) Long-term environmental impact of underground disposal of P&T waste

Voltolini M, Ajo-Franklin JB (2020) The sealing mechanisms of a fracture in opalinus clay as revealed by in situ synchrotron X-ray micro-tomography. Front Earth Sci 8:207

Wiseall AC, Cuss RJ, Graham CC, Harrington JF (2015) The visualization of flow paths in experimental studies of clay-rich materials. Mineral Mag 79(6):1335–1342

Zhang CL (2011) Experimental evidence for self-sealing of fractures in claystone. Phys Chem Earth 36(17–18):1972–1980. https://doi.org/10.1016/j.pce.2011.07.030

Zhang CL, Talandier J (2022) Self-sealing of fractures in indurated claystones measured by water and gas flow. J Rock Mech Geotech Eng. https://doi.org/10.1016/j.jrmge.2022.01.014

Zhang CL, Czaikowski O, Komischke M, Wieczorek K (2014) Thermo-hydro-mechanical processes in the nearfield around a HLW repository in argillaceous formations

Terms and Conditions

Springer Nature journal content, brought to you courtesy of Springer Nature Customer Service Center GmbH (“Springer Nature”).
Springer Nature supports a reasonable amount of sharing of research papers by authors, subscribers and authorised users (“Users”), for small-scale personal, non-commercial use provided that all copyright, trade and service marks and other proprietary notices are maintained. By accessing, sharing, receiving or otherwise using the Springer Nature journal content you agree to these terms of use (“Terms”). For these purposes, Springer Nature considers academic use (by researchers and students) to be non-commercial.
These Terms are supplementary and will apply in addition to any applicable website terms and conditions, a relevant site licence or a personal subscription. These Terms will prevail over any conflict or ambiguity with regards to the relevant terms, a site licence or a personal subscription (to the extent of the conflict or ambiguity only). For Creative Commons-licensed articles, the terms of the Creative Commons license used will apply.
We collect and use personal data to provide access to the Springer Nature journal content. We may also use these personal data internally within ResearchGate and Springer Nature and as agreed share it, in an anonymised way, for purposes of tracking, analysis and reporting. We will not otherwise disclose your personal data outside the ResearchGate or the Springer Nature group of companies unless we have your permission as detailed in the Privacy Policy.
While Users may use the Springer Nature journal content for small scale, personal non-commercial use, it is important to note that Users may not:

1. use such content for the purpose of providing other users with access on a regular or large scale basis or as a means to circumvent access control;
2. use such content where to do so would be considered a criminal or statutory offence in any jurisdiction, or gives rise to civil liability, or is otherwise unlawful;
3. falsely or misleadingly imply or suggest endorsement, approval , sponsorship, or association unless explicitly agreed to by Springer Nature in writing;
4. use bots or other automated methods to access the content or redirect messages
5. override any security feature or exclusionary protocol; or
6. share the content in order to create substitute for Springer Nature products or services or a systematic database of Springer Nature journal content.

In line with the restriction against commercial use, Springer Nature does not permit the creation of a product or service that creates revenue, royalties, rent or income from our content or its inclusion as part of a paid for service or for other commercial gain. Springer Nature journal content cannot be used for inter-library loans and librarians may not upload Springer Nature journal content on a large scale into their, or any other, institutional repository.
These terms of use are reviewed regularly and may be amended at any time. Springer Nature is not obligated to publish any information or content on this website and may remove it or features or functionality at our sole discretion, at any time with or without notice. Springer Nature may revoke this licence to you at any time and remove access to any copies of the Springer Nature journal content which have been saved.
To the fullest extent permitted by law, Springer Nature makes no warranties, representations or guarantees to Users, either express or implied with respect to the Springer nature journal content and all parties disclaim and waive any implied warranties or warranties imposed by law, including merchantability or fitness for any particular purpose.
Please note that these rights do not automatically extend to content, data or other material published by Springer Nature that may be licensed from third parties.
If you would like to use or distribute our Springer Nature journal content to a wider audience or on a regular basis or in any other manner not expressly permitted by these Terms, please contact Springer Nature at

onlineservice@springernature.com